Field Inhomogeneity Correction based on Gridding Reconstruction for Magnetic Resonance Imaging

H. Eggers, T. Knopp, and D. Potts

Abstract—**Spatial variations of the main field give rise to artifacts in magnetic resonance images if disregarded in reconstruction. With non-Cartesian k-space sampling, they often lead to unacceptable blurring. Data from such acquisitions are commonly reconstructed with gridding methods and optionally restored with various correction methods. Both types of methods essentially face the same basic problem of adequately approximating an exponential function to enable an efficient processing with Fast Fourier Transforms. Nevertheless, they have addressed it differently so far. In the present work, a unified approach is proposed. An extension of the principle behind gridding methods is shown to permit its application to field inhomogeneity compensation. Based on this result, several new correction algorithms are derived from a straightforward embedding of the data into a higher dimensional space. They are evaluated in simulations and phantom experiments with spiral k-space sampling. Compared with existing algorithms, one of them promises to provide a favorable compromise between fidelity and complexity. Moreover, it allows a simple choice of key parameters involved in approximating an exponential function and a balance between reconstruction and correction accuracy.**

Index Terms—**Magnetic resonance imaging, image reconstruction, gridding, field inhomogeneity, off-resonance correction, conjugate phase reconstruction, iterative reconstruction, spiral imaging**

I. INTRODUCTION

Magnetic resonance imaging (MRI) relies on a strong, homogeneous main field. While the field strength determines the net magnetization available for signal generation, the field homogeneity ensures adequate coherence between the precession of individual spins within one voxel and thus sufficient signal lifetime for an efficient detection. More subtle variations of the main field between different voxels distort the Fourier encoding used

H. Eggers is with Philips Research, Sector Technical Systems, Hamburg, Germany (e-mail: holger.eggers@philips.com).

T. Knopp is with the Institute of Mathematics, University of Lübeck, Lübeck, Germany (e-mail: knopp@informatik.uni-luebeck.de).

D. Potts is with the Department of Mathematics, Chemnitz University of Technology, Chemnitz, Germany (e-mail: potts@mathematik.tu-chemnitz.de).

to spatially resolve the received signal and lead to artifacts in reconstructed images. These artifacts are mainly limited to geometric distortions and intensity variations for acquisitions with Cartesian k-space trajectories, i.e. which sample the spatial frequency domain of the images on a Cartesian grid. For acquisitions with non-Cartesian k-space trajectories, however, more severe blurring and other artifacts arise. While the inhomogeneity of the main field of today's clinical MRI systems mainly results from susceptibility variations, especially at air-tissue interfaces, the striving for higher field strengths and more open system designs may well render the contribution of the magnet itself once more significant in the future.

The compensation of field inhomogeneity effects in non-Cartesian imaging is usually performed with either a direct conjugate phase reconstruction (CPR) [1] or an iterative algebraic reconstruction [2]. Both are closely related, since one iteration of the latter typically involves the application of the former. The individual methods mainly differ in how they make the distortion of the Fourier encoding, which the field inhomogeneity causes, amenable to a processing with Fast Fourier Transforms (FFTs). They all introduce a coarse segmentation, i.e. discretization, in either k-space or image space and require a separate transformation of each resulting segment. In the corresponding domain, they perform an interpolation to improve accuracy. Among the proposed methods are a Hanning interpolation [1], a linear combination [3], and a least squares combination [4].

If field inhomogeneity effects are disregarded, non-Cartesian acquisitions are commonly reconstructed with gridding methods [5]. These methods have been established as a rapid and robust means of producing images from sets of non-equispaced k-space samples. First, they perform a weighting of the samples to compensate for variations in the sampling density. Then, they convolve them with a window function of finite extent and resample the result to an oversampled Cartesian grid. Finally, they apply an FFT and a deapodization in image space. In this way, gridding methods avoid the use of slow Discrete Fourier Transforms (DFTs) and reach a better compromise between accuracy and complexity than simpler methods that rely on an interpolation in k-

space only.

In fact, the same basic problem underlies both, the compensation of field inhomogeneity effects and the reconstruction of non-Cartesian acquisitions. Nevertheless, it has been addressed differently so far. We propose in this work a unified approach. In the next section, we describe the problem of reconstructing images from non-Cartsian acquisitions in the presence of field inhomogeneity in mathematical terms. We then summarize the non-uniform Fast Fourier Transform (NFFT) and show how it can be adapted for use in field inhomogeneity correction. Based on this result, we derive four new algorithms, which we evaluate in simulations and phantom experiments and compare against existing algorithms. We finally discuss advantages and disadvantages of the proposed approach.

II. THEORY

In MRI, the demodulated signal $s(t)$ received from an object with a magnetization $m(\boldsymbol{r})$ at a reference time point $t = 0$ is ideally given by

$$s(t) = \int_{\mathbb{R}^3} m(\boldsymbol{r})\,\mathrm{e}^{\mathrm{i}\boldsymbol{k}(t)\boldsymbol{r}}\mathrm{d}\boldsymbol{r}\,. \qquad \text{(II.1)}$$

$\boldsymbol{k}(t)$ denotes the trajectory, along which samples are acquired in the spatial frequency domain, the so-called k-space. It is determined by the time variant gradient field applied during the measurement.

Any inhomogeneity of the main field distorts the Fourier encoding that (II.1) describes. Taking this imperfection into account, $s(t)$ is more accurately modelled by

$$s(t) = \int_{\mathbb{R}^3} m(\boldsymbol{r})\,\mathrm{e}^{\mathrm{i}\omega(\boldsymbol{r})t}\mathrm{e}^{\mathrm{i}\boldsymbol{k}(t)\boldsymbol{r}}\mathrm{d}\boldsymbol{r}\,. \qquad \text{(II.2)}$$

$\omega(\boldsymbol{r})$ denotes the angular off-resonance frequency, which is proportional to the local deviation of the main field from its nominal strength. Other imperfections, such as relaxation, are not considered in this work.

From now on we restrict ourselves to 2D imaging. The sampled area of k-space is then confined to $\boldsymbol{k} \in [-\pi, \pi]^2$, and the covered field of view to $\boldsymbol{r} \in [-\frac{N_1}{2}, \frac{N_1}{2}] \times [-\frac{N_2}{2}, \frac{N_2}{2}]$. Discretizing the integral in (II.2) on $N_1 N_2$ equispaced voxel positions $\boldsymbol{r}_\rho$ and the signal $s(t)$ on M time points t_κ yields

$$s_\kappa \approx \tilde{s}_\kappa := \sum_{\rho=0}^{N_1 N_2 - 1} m_\rho \mathrm{e}^{\mathrm{i}\omega_\rho t_\kappa} \mathrm{e}^{\mathrm{i}\boldsymbol{k}_\kappa \boldsymbol{r}_\rho}, \qquad \text{(II.3)}$$

where $s_\kappa := s(t_\kappa)$, $\tilde{s}_\kappa := \tilde{s}(t_\kappa)$, $m_\rho := m(\boldsymbol{r}_\rho)$, $\omega_\rho := \omega(\boldsymbol{r}_\rho)$, and $\boldsymbol{k}_\kappa := \boldsymbol{k}(t_\kappa)$. Using the vectors

$$\boldsymbol{s} := (s_\kappa)_{\kappa=0,\ldots,M-1}\,,$$

$$\boldsymbol{m} := (m_\rho)_{\rho=0,\ldots,N_1 N_2 - 1}\,,$$

and the matrix

$$\boldsymbol{H} := \left(\mathrm{e}^{\mathrm{i}\omega_\rho t_\kappa}\mathrm{e}^{\mathrm{i}\boldsymbol{k}_\kappa \boldsymbol{r}_\rho}\right)_{\kappa=0,\ldots,M-1;\ \rho=0,\ldots,N_1 N_2 - 1}\,,$$

this may be rewritten as

$$\boldsymbol{s} \approx \boldsymbol{H}\boldsymbol{m}\,.$$

We propose determining $\boldsymbol{m}$ by a weighted least squares approach

$$\|\boldsymbol{s} - \boldsymbol{H}\boldsymbol{m}\|_{\boldsymbol{W}} = \sqrt{\sum_{\kappa=0}^{M-1} w_\kappa |s_\kappa - \tilde{s}_\kappa|^2} \xrightarrow{\boldsymbol{m}} \min\,, \quad \text{(II.4)}$$

with factors $w_\kappa > 0$ that compensate for variations in the local sampling density. It leads to the weighted normal equation of first kind

$$\boldsymbol{H}^{\mathsf{H}}\boldsymbol{W}\boldsymbol{H}\boldsymbol{m} = \boldsymbol{H}^{\mathsf{H}}\boldsymbol{W}\boldsymbol{s}\,, \qquad \text{(II.5)}$$

where $\boldsymbol{W} := \mathrm{diag}(w_\kappa)_{\kappa=0,\ldots,M-1}$. Due to the size of this linear system, we suggest to solve it iteratively with a suitable variant of the conjugate gradient method, such as the Conjugate Gradient Normal Equation Residual (CGNR) method. In this way, (II.4) is in each iteration minimized over a certain Krylov space. Moreover, by choosing a zero vector as initial estimate of $\boldsymbol{m}$, the intermediate result after one iteration is identical to that of the CPR, which is one reason for including $\boldsymbol{W}$ in (II.5).

The computational complexity of determining $\boldsymbol{m}$ then depends primarily on two factors, the required number of iterations and the required effort per iteration. The first factor is mostly linked to the employed initial estimate of $\boldsymbol{m}$ and to the condition of $\boldsymbol{H}$. We stick with a zero vector as initial estimate and apply no additional preconditioning in this work, yet the presence of $\boldsymbol{W}$ in (II.5) is also motivated by its beneficial effect on the condition of the system matrix. The second factor is mainly influenced by the multiplication of a vector with the matrix $\boldsymbol{H}$ or $\boldsymbol{H}^{\mathsf{H}}$. Due to the distorted Fourier encoding, this matrix-vector product may not simply be implemented with a standard FFT. As we will show in the next but one subsection, it may be realized with a modified NFFT, however.

A. NFFT

The standard NFFT permits the fast, approximate evaluation of the Fourier transform of a vector of equispaced samples at a vector of non-equispaced positions. We briefly summarize it in this subsection for the one dimensional case. The reader is referred to [6] for a more detailed description.

Let a function $\varphi \in L^2(\mathbb{R}) \cap L^1(\mathbb{R})$, the so-called window function, be given. Its one periodization

$$\tilde{\varphi}(k) := \sum_{p=-\infty}^{\infty} \varphi(k+p)$$

is assumed to have a uniformly convergent Fourier series. Hence, it may be written as

$$\tilde{\varphi}(k) = \sum_{x=-\infty}^{\infty} c_x(\tilde{\varphi}) e^{2\pi i k x} ,$$

with Fourier coefficients

$$c_x(\tilde{\varphi}) := \int_{-1/2}^{1/2} \tilde{\varphi}(k) e^{-2\pi i k x} \, dk , \qquad (\text{II.6})$$

where $x \in \mathbb{Z}$. Substituting k by $k - k'$ in (II.6) yields

$$c_x(\tilde{\varphi}) = \int_{-1/2}^{1/2} \tilde{\varphi}(k - k') e^{-2\pi i (k-k') x} \, dk' , \qquad (\text{II.7})$$

which may be approximated by

$$c_x(\tilde{\varphi}) \approx \frac{1}{\alpha N} \sum_{l=-\alpha N/2}^{\alpha N/2-1} \tilde{\varphi}(k - \frac{l}{\alpha N}) e^{-2\pi i (k - \frac{l}{\alpha N}) x} \quad (\text{II.8})$$

for $k \in [-\frac{1}{2}, \frac{1}{2}]$ and $x = -\frac{N}{2}, \ldots, \frac{N}{2}$. The factor $\alpha > 1$ is commonly referred to as oversampling factor. For the sake of simplicity, N and αN are assumed to be even. Provided that all $c_x(\tilde{\varphi})$ are unequal zero, (II.8) may be rewritten as

$$e^{2\pi i k x} \approx \frac{1}{\alpha N c_x(\tilde{\varphi})} \sum_{l=-\alpha N/2}^{\alpha N/2-1} \tilde{\psi}(k - \frac{l}{\alpha N}) e^{2\pi i \frac{lx}{\alpha N}} , \quad (\text{II.9})$$

where $\tilde{\varphi}$ has been replaced by $\tilde{\psi}$. The latter is the one periodization of a truncation of φ defined by

$$\psi(k) := \begin{cases} \varphi(k) & k \in [-\frac{m}{\alpha N}, \frac{m}{\alpha N}], \\ 0 & k \notin [-\frac{m}{\alpha N}, \frac{m}{\alpha N}]. \end{cases}$$

The support of ψ is determined by $2m$, the so-called kernel size. Typically, $m \in \mathbb{N}$ is chosen such that $m \ll N$.

The standard NFFT evaluates the trigonometric polynomial

$$f(k) := \sum_{x=-N/2}^{N/2-1} \hat{f}_x e^{2\pi i k x} \qquad (\text{II.10})$$

for N given equispaced samples $\hat{f}_x$ at M given non-equispaced positions $k_j \in [-\frac{1}{2}, \frac{1}{2}]$. It uses the approximation (II.9), which yields

$$f_j \approx \sum_{l=-\alpha N/2}^{\alpha N/2-1} \tilde{\psi}(k_j - \frac{l}{\alpha N}) \sum_{x=-N/2}^{N/2-1} \frac{\hat{f}_x}{\alpha N c_x(\tilde{\varphi})} \times e^{2\pi i \frac{lx}{\alpha N}} , \qquad (\text{II.11})$$

where $f_j := f(k_j)$. In matrix-vector notation, (II.10) then reads

$$\boldsymbol{f} = \boldsymbol{A}\hat{\boldsymbol{f}} , \qquad (\text{II.12})$$

with

$$\boldsymbol{f} := (f_j)_{j=0,\ldots,M-1} ,$$

$$\hat{\boldsymbol{f}} := \left(\hat{f}_x \right)_{x=-N/2,\ldots,N/2-1} ,$$

$$\boldsymbol{A} := \left(e^{2\pi i k_j x} \right)_{j=0,\ldots,M-1; \; x=-N/2,\ldots,N/2-1} .$$

According to (II.11), $\boldsymbol{A}$ may be approximated by $\boldsymbol{BFD}$, where $\boldsymbol{D}$ is a diagonal matrix with entries $d_{x,x} = 1/c_x(\tilde{\varphi})$, $\boldsymbol{F}$ an oversampled Fourier matrix, which includes the factor $1/(\alpha N)$, and $\boldsymbol{B}$ a sparse matrix with entries $b_{j,l} = \tilde{\psi}(k_j - l/(\alpha N))$. Similarly, the evaluation of the adjoint to (II.10), i.e. of the sum

$$\sum_{j=0}^{M-1} f_j e^{-2\pi i k_j x}$$

for M given non-equispaced samples f_j at N given equispaced positions $x = -\frac{N}{2}, \ldots, \frac{N}{2} - 1$, may be performed by a matrix-vector multiplication with $\boldsymbol{A}^{\boldsymbol{\dashv}} \approx \boldsymbol{D}^{\boldsymbol{\dashv}} \boldsymbol{F}^{\boldsymbol{\dashv}} \boldsymbol{B}^{\boldsymbol{\dashv}}$. As pointed out in [6], [7], gridding reconstruction is simply a fast algorithm for the application of $\boldsymbol{D}^{\boldsymbol{\dashv}} \boldsymbol{F}^{\boldsymbol{\dashv}} \boldsymbol{B}^{\boldsymbol{\dashv}}$ to a vector of non-equispaced samples. Including a sampling density compensation, it involves [5]

1) a weighting of the data, i.e. a multiplication with $\boldsymbol{W}$,
2) a convolution with a window function and a re-sampling to an oversampled Cartesian grid, i.e. a multiplication with $\boldsymbol{B}^{\boldsymbol{\dashv}}$,
3) an inverse FFT, i.e. a multiplication with $\boldsymbol{F}^{\boldsymbol{\dashv}}$,
4) a deapodization, i.e. a multiplication with $\boldsymbol{D}^{\boldsymbol{\dashv}}$.

Unified approaches to the efficient computation of (II.10) or (II.12) with the NFFT were suggested in [6], [8]. We follow in this work the former, which permits a simple change of the window function. Among the various functions proposed for φ, the Kaiser-Bessel window, or its Fourier transform, turned out to be a particularly good choice. More sophisticated approaches based on scaling vectors [9], a minimization of the Frobenius norm

of certain error matrices [10], or a min-max interpolation [11] did not prove significantly superior.

Obviously, the NFFT and gridding reconstruction not only involve closely related processing, but also exploit the same approximation. To address field inhomogeneity correction similarly, we conclude this subsection with the derivation of an approximation that lifts the restriction on x to be an integer in (II.9). Starting from

$$\hat{\varphi}(x) := \int\limits_{-\infty}^{\infty} \varphi(k)\mathrm{e}^{-2\pi\mathrm{i}kx}\,\mathrm{d}k$$

instead of (II.6) leads to

$$\hat{\varphi}(x) = \int\limits_{-1/2}^{1/2} \sum_{p=-\infty}^{\infty} \varphi(k+p)\mathrm{e}^{-2\pi\mathrm{i}(k+p)x}\,\mathrm{d}k$$

and, with the same steps as from (II.7) to (II.9), to

$$\mathrm{e}^{2\pi\mathrm{i}kx} \approx \frac{1}{\alpha N\hat{\varphi}(x)}\sum_{l=-\alpha N/2}^{\alpha N/2-1}\sum_{p=-\infty}^{\infty} \psi\left(k - \frac{l}{\alpha N} + p\right)$$
$$\times\mathrm{e}^{2\pi\mathrm{i}\left(\frac{l}{\alpha N}+p\right)x}$$

for $k \in [-\frac{1}{2}, \frac{1}{2}]$ and $x \in [-\frac{N}{2}, \frac{N}{2}]$. Like (II.9), this approximation may be reduced to

$$\mathrm{e}^{2\pi\mathrm{i}kx} \approx \frac{1}{\alpha N\hat{\varphi}(x)}\sum_{l=-\alpha N/2}^{\alpha N/2-1} \psi\left(k - \frac{l}{\alpha N}\right)\mathrm{e}^{2\pi\mathrm{i}\frac{lx}{\alpha N}} \quad \text{(II.13)}$$

for $k \in [-\frac{1}{2} + \frac{m}{\alpha N}, \frac{1}{2} - \frac{m}{\alpha N}]$, since the support of ψ is $[-\frac{m}{\alpha N}, \frac{m}{\alpha N}]$. Consequently, (II.13) is a good approximation if $kx \in [-\frac{N}{4} + \frac{m}{2\alpha}, \frac{N}{4} - \frac{m}{2\alpha}]$. It is worth noting that the further restriction of k may in principle be avoided by explicitly taking the periodization into account. We will not explore this alternative in the present work, however.

B. Matrix-vector product

To efficiently multiply a vector with the matrix $\boldsymbol{H}$ or $\boldsymbol{H}^{\boldsymbol{\mathsf{H}}}$, we start off by embedding the data in both domains in a higher dimensional space [12]. For this purpose, we set $\boldsymbol{k}'_\kappa = ((\boldsymbol{k}_\kappa)^\top, t_\kappa)^\top$ and $\boldsymbol{r}'_\rho = ((\boldsymbol{r}_\rho)^\top, \omega_\rho)^\top$, i.e. we add a time dimension to the frequency domain and an off-resonance frequency dimension to the spatial domain. (II.3) may then be rewritten as

$$s_\kappa \approx \sum_{\rho=0}^{N_1 N_2-1} m_\rho \mathrm{e}^{\mathrm{i}\boldsymbol{k}'_\kappa \boldsymbol{r}'_\rho}. \quad \text{(II.14)}$$

A straightforward evaluation of this sum with the standard NFFT is not possible, since the samples in neither domain are equispaced. However, a so-called NNFFT was first suggested in [13] and later studied in more depth in [14], which permits the fast calculation of the Fourier transform of a vector of non-equispaced samples at a vector of non-equispaced positions. It constitutes a combination of the standard NFFT and its adjoint. Applying it to the computation of (II.14), an approach we will call 3D NNFFT, entails a 3D FFT and in both domains a 3D convolution with a window function. Additionally, it demands two multiplicative oversampling factors, which increase the length of the Fourier transform in all three dimensions. The evaluation of the adjoint, i.e. of the sum

$$\sum_{\kappa=0}^{M-1} s_\kappa \mathrm{e}^{-\mathrm{i}\boldsymbol{k}'_\kappa \boldsymbol{r}'_\rho},$$

involves the same effort.

To employ the standard NFFT instead, we have to resample the data in one domain to a Cartesian grid. We achieve this by using the approximation (II.13). Since this step is unnecessary for $\boldsymbol{r}$, preferably the spatial domain is resampled. We first choose an integer constant N_3 such that

$$\frac{\omega_\rho t_\kappa}{2\pi} \in [-\frac{N_3}{4} + \frac{m}{2\alpha}, \frac{N_3}{4} - \frac{m}{2\alpha}]$$

for all ρ and κ. As the complexity of the matrix-vector product grows with N_3, it should be kept as small as possible. Centering both ω_ρ and t_κ, which involves a multiplication of the input and output data with a phase, is, therefore, advantageous. We further define a scaling factor W such that

$$\frac{\omega_\rho}{W} \in [-\frac{1}{2} + \frac{m}{\alpha N_3}, \frac{1}{2} - \frac{m}{\alpha N_3}]$$

for all ρ. With the approximation (II.13), we then obtain

$$\mathrm{e}^{\mathrm{i}\omega_\rho t_\kappa} = \mathrm{e}^{2\pi\mathrm{i}\frac{\omega_\rho}{W}\frac{W t_\kappa}{2\pi}}$$
$$\approx \frac{1}{\alpha N_3\hat{\varphi}\left(\frac{W t_\kappa}{2\pi}\right)}\sum_{l=-\alpha N_3/2}^{\alpha N_3/2-1} \psi\left(\frac{\omega_\rho}{W} - \frac{l}{\alpha N_3}\right)$$
$$\times\mathrm{e}^{\mathrm{i}\frac{W t_\kappa l}{\alpha N_3}}.$$

Insertion into (II.3) yields

$$s_\kappa \approx \frac{1}{\alpha N_3\hat{\varphi}\left(\frac{W t_\kappa}{2\pi}\right)}\sum_{l=-\alpha N_3/2}^{\alpha N_3/2-1}\sum_{\rho=0}^{N_1 N_2-1} m_\rho \psi\left(\frac{\omega_\rho}{W} - \frac{l}{\alpha N_3}\right)$$
$$\times\mathrm{e}^{\mathrm{i}\boldsymbol{k}_\kappa \boldsymbol{r}_\rho}\mathrm{e}^{\mathrm{i}\frac{W t_\kappa l}{\alpha N_3}}. \quad \text{(II.15)}$$

With $\boldsymbol{k}''_\kappa := (\boldsymbol{k}_\kappa^\top, W t_\kappa/(\alpha N_3))^\top$ and $\boldsymbol{r}''_{(\rho,l)} := ((\boldsymbol{r}_\rho)^\top, l)^\top$, we finally get

$$s_\kappa \approx \frac{1}{\alpha N_3\hat{\varphi}\left(\frac{W t_\kappa}{2\pi}\right)}\sum_{l=-\alpha N_3/2}^{\alpha N_3/2-1}\sum_{\rho=0}^{N_1 N_2-1} m_\rho \psi\left(\frac{\omega_\rho}{W} - \frac{l}{\alpha N_3}\right)$$
$$\times\mathrm{e}^{\mathrm{i}\boldsymbol{k}''_\kappa \boldsymbol{r}''_{(\rho,l)}}.$$

The matrix-vector product may thus be realized by a 3D NFFT. Hence, we will call this approach 3D NFFT. It requires a 3D FFT and a 3D convolution with a window function in the frequency domain, and it introduces two multiplicative oversampling factors only for the added third dimension. The adjoint reads

$$\sum_{l=-\alpha N_3/2}^{\alpha N_3/2-1} \psi\left(\frac{\omega_\rho}{W} - \frac{l}{\alpha N_3}\right) \sum_{\kappa=0}^{M-1} \frac{s_\kappa}{\alpha N_3 \hat{\varphi}\left(-\frac{W t_\kappa}{2\pi}\right)} e^{-i\boldsymbol{k}_\kappa'' \boldsymbol{r}_{(\rho,l)}''}$$

and may also be computed with a 3D NFFT, but additionally with a sparse summation over l.

We now consider separating the 3D domains into 2D⊗1D domains. In this way, the Fourier transform of the added third dimension can be replaced by an explicit sum, which appears beneficial in view of the sparseness of the data in the 3D spaces. By merely rearranging (II.15), we obtain

$$\begin{aligned} s_\kappa &\approx \sum_{l=-\alpha N_3/2}^{\alpha N_3/2-1} \frac{e^{i\frac{W t_\kappa l}{\alpha N_3}}}{\alpha N_3 \hat{\varphi}\left(\frac{W t_\kappa}{2\pi}\right)} \sum_{\rho=0}^{N_1 N_2-1} m_\rho \psi\left(\frac{\omega_\rho}{W} - \frac{l}{\alpha N_3}\right) \\ &\times e^{i\boldsymbol{k}_\kappa \boldsymbol{r}_\rho}. \end{aligned}$$

With this approximation, the matrix-vector product may be calculated by N_3 2D NFFTs and a summation over l, an approach we will call 2D⊗1D NFFT-F. It involves a 2D FFT and a 2D convolution with a window function in the frequency domain for each NFFT, and it demands only one oversampling factor in each dimension. The adjoint is given by

$$\sum_{l=-\alpha N_3/2}^{\alpha N_3/2-1} \psi\left(\frac{\omega_\rho}{W} - \frac{l}{\alpha N_3}\right) \sum_{\kappa=0}^{M-1} \frac{s_\kappa e^{-i\frac{W t_\kappa l}{\alpha N_3}}}{\alpha N_3 \hat{\varphi}\left(-\frac{W t_\kappa}{2\pi}\right)} e^{-i\boldsymbol{k}_\kappa \boldsymbol{r}_\rho},$$

where the summation over l is sparse.

We derive a variant of this approach by defining another scaling factor T such that

$$\frac{t_\kappa}{T} \in \left[-\frac{1}{2} + \frac{m}{\alpha N_3}, \frac{1}{2} - \frac{m}{\alpha N_3}\right]$$

for all κ. Using the approximation (II.13), we get

$$\begin{aligned} e^{i\omega_\rho t_\kappa} &= e^{2\pi i \frac{t_\kappa}{T} \frac{\omega_\rho T}{2\pi}} \\ &\approx \frac{1}{\alpha N_3 \hat{\varphi}\left(\frac{\omega_\rho T}{2\pi}\right)} \sum_{l=-\alpha N_3/2}^{\alpha N_3/2-1} \psi\left(\frac{t_\kappa}{T} - \frac{l}{\alpha N_3}\right) \\ &\times e^{i\frac{\omega_\rho T l}{\alpha N_3}}. \end{aligned}$$

Insertion into (II.3) yields

$$\begin{aligned} s_\kappa &\approx \sum_{l=-\alpha N_3/2}^{\alpha N_3/2-1} \psi\left(\frac{t_\kappa}{T} - \frac{l}{\alpha N_3}\right) \sum_{\rho=0}^{N_1 N_2-1} \frac{m_\rho e^{i\frac{\omega_\rho T l}{\alpha N_3}}}{\alpha N_3 \hat{\varphi}\left(\frac{\omega_\rho T}{2\pi}\right)} \\ &\times e^{i\boldsymbol{k}_\kappa \boldsymbol{r}_\rho}. \end{aligned}$$

In this way, the matrix-vector product may again be computed by N_3 2D NFFTs, followed by a sparse summation over l, an approach we will call 2D⊗1D NFFT-T. The effort for the NFFTs is substantially reduced if they are evaluated only at those k-space positions that actually contribute to the sparse summation. For the adjoint

$$\sum_{l=-\alpha N_3/2}^{\alpha N_3/2-1} \frac{e^{-i\frac{\omega_\rho T l}{\alpha N_3}}}{\alpha N_3 \hat{\varphi}\left(-\frac{\omega_\rho T}{2\pi}\right)} \sum_{\kappa=0}^{M-1} s_\kappa \psi\left(\frac{t_\kappa}{T} - \frac{l}{\alpha N_3}\right) e^{-i\boldsymbol{k}_\kappa \boldsymbol{r}_\rho},$$

the summation over l is no longer sparse, but the effort for the NFFTs may be decreased similarly.

With respect to computational complexity, we conclude that the 2D⊗1D NFFT-T approach is the most efficient, followed by the 2D⊗1D NFFT-F and the 3D NFFT approach. This ranking will, together with an experimental comparison of accuracy, guide the selection of the best of these gridding-based field inhomogeneity correction algorithms.

III. METHODS

We assessed the four proposed algorithms in simulations and phantom experiments using spiral k-space sampling.

A. Simulations

The simulations were based on a Shepp-Logan phantom with a resolution of 256 x 256, to which a slightly smoothed circular shutter with a radius of $\frac{7}{8}\pi$ was applied in k-space. In this way, we took into account that spiral acquisitions sample only a circular area in k-space and that field inhomogeneity leads to an additional signal modulation, which seemingly spreads the spatial frequency spectrum of an image over time. The radius of this shutter was chosen such that most of the energy remained within the covered circular area in k-space throughout the acquisition window. In addition, the two field maps displayed in Fig. V.1 were used. One reflects a continuous, parabolic variation of the main field strength, the other a discrete, linear one. Both span the same range of off-resonance frequencies.

k-space data were calculated by a direct evaluation of (II.3). The acquisition was segmented into 12 spiral interleaves with 13332 samples each, including a twofold oversampling. Two images obtained with a standard gridding reconstruction of these data, i.e. without field inhomogeneity correction, are presented in Fig. V.1. An analytical function described in [15] served the sampling density compensation in this case. Obviously, both field distributions give rise to blurring, but discontinuities cause additional, major artifacts.

Next to the proposed gridding-based ones, a number of existing field inhomogeneity correction algorithms were implemented as reference. These included a nearest neighbor interpolation with frequency segmentation [16], a Hanning interpolation with time segmentation [1], and the more sophisticated Man [3], [17] and least squares [3], [4] interpolations, both with time and frequency segmentation. For the Man interpolation with time segmentation, a manual variation of the oversampling factor was performed, since no explicit rule for its choice was known. For the least squares interpolation, a Householder transformation was employed to solve the occurring minimization problems. All of these algorithms fit in the same, general framework outlined in [17], which approximates (II.3) by a linear combination of differently weighted, transformed and resampled images.

Reconstruction results were assessed both visually and quantitatively. As measure, we used the sum of squares of the differences between reconstructed and original image pixels, divided by the sum of squares of the original image pixels.

All algorithms were implemented both in Matlab and in C. They were tested on a conventional workstation equipped with an Intel Xeon processor running at 2 GHz and with 256 MB of memory. The software configuration used was Linux 2.4.21, FFTW 3.0.1, and NFFT 2.0. The latter is available from [18] and essentially differs from a standard gridding reconstruction in two respects only: Instead of a Kaiser-Bessel window, its Fourier transform is employed as window function, and its shape parameter is well defined.

B. Experiments

The experiments were performed on a 1.5 T Achieva whole-body scanner (Philips Medical Systems, Best, The Netherlands). Transversal cross sections of standard imaging phantoms were acquired with a resolution of 256 x 256 pixels using a segmented spiral gradient echo sequence. A field of view of 250 mm, a slice thickness of 10 mm, a flip angle of $90°$, a TE of 2 ms, and a TR of 1 s were chosen. The readout duration, i.e. the length of time that data are acquired after each excitation, varied between 10 ms and 60 ms, and the number of spiral interleaves changed accordingly.

Field maps were obtained from two separate measurements, which usually differed in TE by 1 ms. Two images were reconstructed from them and thresholded based on signal intensity. Their phases were then subtracted and the differences scaled and slightly filtered. To reduce edge effects, the resulting field maps were additionally extrapolated to areas masked out before.

IV. RESULTS

A. Simulations

The four proposed gridding-based field inhomogeneity correction algorithms are analyzed regarding their accuracy in Tab. V.1. These simulations were performed with the continuous field map and the settings $\alpha = 1.25$, $m = 2$, and $\alpha N_3 = 14$. After one iteration, all four algorithms yield similar errors, i.e. they achieve a comparable accuracy when being applied in a CPR. After three iterations, the 3D NNFFT approach produces an about 100% and the 2D⊗1D NFFT-F approach an about 20% higher error than the two others. Beyond three iterations, errors did not decrease significantly anymore. In view of the discussed differences in computational complexity, the 2D⊗1D NFFT-T approach seems to be the preferred of the four proposed algorithms.

The performance of the 2D⊗1D NFFT-T approach is demonstrated with two examples in Fig. V.2. For the continuous field map, already the first iteration yields a visually good result. Mainly the second iteration provides further improvements, primarily at edges. For the discrete field map, the first iteration produces a visually unacceptable result due to strong artifacts arising from discontinuities. These artifacts are dramatically reduced after a second iteration, but it takes about ten iterations, before the shape of the field map is no longer discernible in the resulting image. This difference in convergence is in good agreement with earlier work, which showed that for spiral k-space sampling the CPR works reasonably well only if the field map is smooth [17], [19].

The accuracy of the 2D⊗1D NFFT-T approach is compared to that of established field inhomogeneity correction algorithms in Fig. V.3. The simulations were agained performed with the continuous field map, and the settings for the NFFT applied to the two standard dimensions were $\alpha = 1.25$ and $m = 2$. Shown are results for one iteration, i.e. the CPR, and three iterations. Those for the least squares algorithm were obtained with a time segmentation. Using a frequency segmentation instead, errors increased for low number of segments and remained comparable for high number of segments. For the gridding-based approach, α and m were matched to the respective αN_3. As for the Man interpolation, the approximation becomes senseless below a certain minimum number of segments, which is 8 in this case. Although slightly lower errors were achieved with a time segmentation, the presented results for the Man interpolation were obtained with a frequency segmentation, since it required no manual tuning of the oversampling factor. The nearest neighbor interpolation with frequency segmentation was not included in the graphs, since it

basically failed to yield acceptable results for more than one iteration. While the least squares algorithm obviously achieves the lowest error of all, the gridding-based approach reaches comparable levels very rapidly for a sufficiently large kernel size and oversampling factor. Using, for instance, the same settings as for the NFFT applied to the two standard dimensions, αN_3 is 14. The least squares and the gridding-based algorithms provide similar accuracy in this case. Moreover, the overall accuracy is limited by the NFFT applied to the two standard dimensions beyond this point, since errors no longer decrease significantly for higher number of segments. The Man interpolation achieves reasonably good results for one iteration, but takes a high number of segments to reach an adequate accuracy for three iterations. The Hanning interpolation performs poorest, except for very low number of segments, where both the Man interpolation and the gridding-based approach fail to provide a useful approximation.

The running times per iteration of the same four correction algorithms are summarized in V.2. In all cases, the number of segments was 14, and the oversampling factor was 1.25. Not included in the running times is the initialization. The differences are, therefore, due to varying amounts of data that are to be regridded per iteration. These amounts are determined by the number of non-zero linear combination coefficients. The least squares and the Man interpolation show the longest running times, since all coefficients are non-zero. By contrast, only a maximum of $2m + 1$ out of each αN_3 coefficients are non-zero using the gridding-based approach, and only a maximum of 3 using the Hanning interpolation. Consequently, both exhibit significantly shorter running times.

B. Experiments

Representative results of the phantom experiments are summarized in Fig. V.4. The off-resonance frequencies covered a range of 210 Hz in this example. Using 12 spiral interleaves and an acquisition window length of 28.5 ms, the gridding-based field inhomogeneity correction yields an almost perfect image after three iterations. The number of segments was 12 in this case, corresponding to $\alpha = 1.33$. Using 6 spiral interleaves and an acquisition window length of 56.5 ms, the proposed algorithm still provides an image of good overall quality, although residual artifacts remain visible, in particular near the circumference and the resolution rods of the phantom. The number of segments was 19 in this case, corresponding to $\alpha = 1.26$.

V. DISCUSSION

The efficient reconstruction of non-Cartesian acquisitions faces the problem of a non-equispaced sampling in k-space. It is adequately solved by the basic approximation underlying the gridding methods (II.9). Field inhomogeneity, however, introduces an exponential function into the forward model that is irregularly sampled in both the frequency and the time domain. We showed that (II.9) can be adapted to this case, leading to the similar approximation (II.13). In this way, the reconstruction and the field inhomogeneity correction of non-Cartesian acquisitions may be founded on the same basic approximation. This allows to achieve more simply a balance between reconstruction and correction accuracy. From this result, we have derived four new algorithms for the compensation of field inhomogeneity effects.

Among the proposed algorithms, the 3D NNFFT approach shows the highest error. We attribute this to the unnecessary regridding of all spatial dimensions, which involves an approximation. Explicitly using the knowledge that the image is discretized on a Cartesian grid obviously pays off. The slight preference for a time segmentation over a frequency segmentation, both visually and quantitatively, was also found for the other, existing algorithms. Performing the interpolation in the transformed domain of the final result, i.e. in the spatial frequency domain of the image to be reconstructed, generally seems to reduce the perceived artifact level. We selected the 2D⊗1D NFFT-T approach for further investigations mainly due to its lower computational complexity. However, the 3D NFFT approach achieves a similar accuracy and is conceptually far simpler.

The comparison in Fig. V.3 shows that the combination of a local convolution and a convolution correction in the transformed domain, as used by the gridding-based approach, clearly outperforms a mere interpolation in one domain. The Hanning and the Man interpolation achieve only a substantially lower accuracy beyond a certain number of segments. The proposed gridding-based approach permits an explicit calculation of this bound, above which it reaches an accuracy comparable to that of the least squares approach.

The comparison of the running times highlighted the relevance of the amount of data to be regridded. Therefore, the use of a local neighborhood in the interpolation is again advantageous, similar as in standard gridding. Previously, it has been proposed to essentially eliminate most of the regridding from both the conjugate phase [17] and the algebraic [20] reconstruction. While a detailed comparison remains to be done, the apparent

advantage is often offset by either a restriction on the supported k-space trajectories or the requirement of higher oversampling factors to avoid excessive backfolding, as demonstrated for a related problem in parallel imaging [21].

Another crucial factor is the effort involved in the initialization, which is mainly determined by the calculation of the weights for the linear combination from a given field map. Among the compared correction algorithms, those that require little such effort are clearly preferable for small number of iterations. The additional initial effort involved in, for instance, least squares interpolation usually pays off for large number of iterations only.

TABLE AND FIGURE CAPTIONS

Tab. IV.1. Comparison of the accuracy of different gridding-based correction algorithms. Listed is the normalized root mean square (RMS) error after 1, 2, and 3 iterations.

Tab. IV.2. Comparison of the running times of different correction algorithms. Listed is the measured computation time per iteration, using comparable parameter settings.

Fig. III.1. Image and field maps used in simulations. Shown are a filtered Shepp-Logan phantom on the left, a continuous, parabolic and a discrete, linear field map with off-resonance frequencies in the range of -125 Hz to +125 Hz in the middle, and results of a standard gridding reconstruction on the right. The latter were obtained from simulations of spiral k-space sampling and a readout duration of 32 ms. The dashed line superimposed on the phantom indicates the position where cross sections were taken for comparison.

Fig. IV.1. Results of simulations. Shown are intermediate images after 1, 2, and 3 iterations for the continuous field map at the top and after 1, 2, and 10 iterations for the discrete field map at the bottom. Below them, the differences to the original phantom are plotted for one cross section. The scaling varies by one order of magnitude between those at the top and those at the bottom.

Fig. IV.2. Comparison of the accuracy of different correction algorithms. Plotted is the normalized root mean square (RMS) error as function of the number of segments in the interpolation after 1 and 3 iterations on the left and on the right, respectively.

Fig. IV.3. Results of phantom experiments. Shown are a reference image and a field map obtained with Cartesian k-space sampling on the left, and two corresponding uncorrected and corrected images obtained with spiral k-space sampling. Those in the middle were measured with a readout duration of 28.5 ms, and those on the right with a readout duration of 56.5 ms.

REFERENCES

[1] D. C. Noll, C. H. Meyer, J. M. Pauly, D. G. Nishimura, and A. Macovski, "A homogeneity correction method for magnetic resonance imaging with time-varying gradients," IEEE *Trans. Med. Imag.*, vol. 10, pp. 629 – 637, 1991.

[2] Y. M. Kadah and X. Hu, "Algebraic reconstruction for magnetic resonance imaging under B_0 inhomogeneity," IEEE *Trans. Med. Imag.*, vol. 17, pp. 362 – 370, 1998.

[3] L.-C. Man, J. M. Pauly, and A. Macovski, "Multifrequency interpolation for fast off-resonance correction," *Magn. Reson. Med.*, vol. 37, pp. 785 – 792, 1997.

[4] B. P. Sutton, D. C. Noll, and J. A. Fessler, "Fast, iterative image reconstruction for MRI in the presence of field inhomogeneities," IEEE *Trans. Med. Imag.*, vol. 22, pp. 178 – 188, 2003.

[5] J. D. O'Sullivan, "A fast sinc function gridding algorithm for Fourier inversion in computer tomography," IEEE *Trans. Med. Imag.*, vol. 4, pp. 200 – 207, 1985.

[6] D. Potts, G. Steidl, and M. Tasche, "Fast Fourier Transforms for nonequispaced data: A tutorial," in *Modern Sampling Theory: Mathematics and Applications*, J. J. Benedetto and P. J. S. G. Ferreira, Eds. Boston: Birkhäuser, 2001, pp. 247 – 270.

[7] G. E. Sarty, R. Bennett, and R. W. Cox, "Direct reconstruction of non-Cartesian k-space data using a nonuniform Fast Fourier Transform," *Magn. Reson. Med.*, vol. 45, pp. 908 – 915, 2001.

[8] G. Steidl, "A note on Fast Fourier Transforms for nonequispaced grids," *Adv. Comput. Math.*, vol. 9, pp. 337 – 353, 1998.

[9] N. Nguyen and Q. H. Liu, "The regular Fourier matrices and nonuniform Fast Fourier Transforms," SIAM *J. Sci. Comput.*, vol. 21, pp. 283 – 293, 1999.

[10] A. Nieslony and G. Steidl, "Approximate factorizations of Fourier matrices with nonequispaced knots," *Linear Algebra Appl.*, vol. 266, pp. 337 – 351, 2003.

[11] J. A. Fessler and B. P. Sutton, "Nonuniform Fast Fourier Transforms using min-max interpolation," IEEE *Trans. Signal Process.*, vol. 51, pp. 560 – 574, 2003.

[12] J.-Y. Lee and L. Greengard, "The type 3 nonuniform FFT and its applications," *J. Comput. Physics*, vol. 206, pp. 1 – 5, 2005.

[13] A. Dutt and V. Rokhlin, "Fast Fourier Transforms for nonequispaced data," SIAM *J. Sci. Stat. Comput.*, vol. 14, pp. 1368 – 1393, 1993.

[14] B. Elbel and G. Steidl, "Fast Fourier Transforms for nonequispaced data," in *Approximation Theory IX*, C. K. Chui and L. L. Schumaker, Eds. Nashville: Vanderbilt University Press, 1998, pp. 39 – 46.

[15] R. D. Hoge, R. K. Kwan, and G. B. Pike, "Density compensation functions for spiral MRI," *Magn Reson Med*, vol. 38, pp. 117–128, 1997.

[16] D. C. Noll, J. M. Pauly, C. H. Meyer, D. G. Nishimura, and A. Macovski, "Deblurring for non-2D Fourier transform magnetic resonance imaging," *Magn. Reson. Med.*, vol. 25, pp. 319 – 333, 1992.

[17] H. Schomberg, "Off-resonance correction of MR images," IEEE *Trans. Med. Imag.*, vol. 18, pp. 481 – 495, 1999.

[18] S. Kunis and D. Potts. (2005, Apr.) NFFT 2.0, C subroutine library. [Online]. Available: http://www.math.uni-luebeck.de/potts/nfft

[19] T. B. Harshbarger and D. B. Twieg, "Iterative reconstruction of single-shot spiral MRI with off-resonance," IEEE *Trans. Med. Imag.*, vol. 18, pp. 196 – 205, 1999.

[20] J. A. Fessler, S. Lee, V. T. Olafsson, H. R. Shi, and D. C. Noll, "Toeplitz-based iterative image reconstruction for MRI with correction for magnetic field inhomogeneity," IEEE *Trans. Sig. Proc.*, vol. 53, pp. 3393 – 3402, 2005.

[21] H. Eggers, P. Boernert, and P. Boesiger, "Comparison of gridding- and convolution-based iterative reconstruction algorithms for sensitivity-encoded non-Cartesian acquisitions," in *Proc. ISMRM*, 2002, p. 743.

Iteration	1	2	3
3D NNFFT	$5.41 \cdot 10^{-2}$	$1.15 \cdot 10^{-2}$	$1.13 \cdot 10^{-2}$
3D NFFT	$5.31 \cdot 10^{-2}$	$5.83 \cdot 10^{-3}$	$5.42 \cdot 10^{-3}$
2D⊗1D NFFT-F	$5.39 \cdot 10^{-2}$	$6.99 \cdot 10^{-3}$	$6.39 \cdot 10^{-3}$
2D⊗1D NFFT-T	$5.32 \cdot 10^{-2}$	$5.50 \cdot 10^{-3}$	$5.21 \cdot 10^{-3}$

TABLE V.1

COMPARISON OF THE ACCURACY OF DIFFERENT GRIDDING-BASED CORRECTION ALGORITHMS. LISTED IS THE NORMALIZED ROOT MEAN SQUARE (RMS) ERROR AFTER 1, 2, AND 3 ITERATIONS.

Algorithm	Running Time
Least squares	1530 ms
Gridding-based (2D⊗1D NFFT-T)	840 ms
Man	1530 ms
Hanning	710 ms

TABLE V.2

COMPARISON OF THE RUNNING TIMES OF DIFFERENT CORRECTION ALGORITHMS. LISTED IS THE MEASURED COMPUTATION TIME PER ITERATION, USING COMPARABLE PARAMETER SETTINGS.
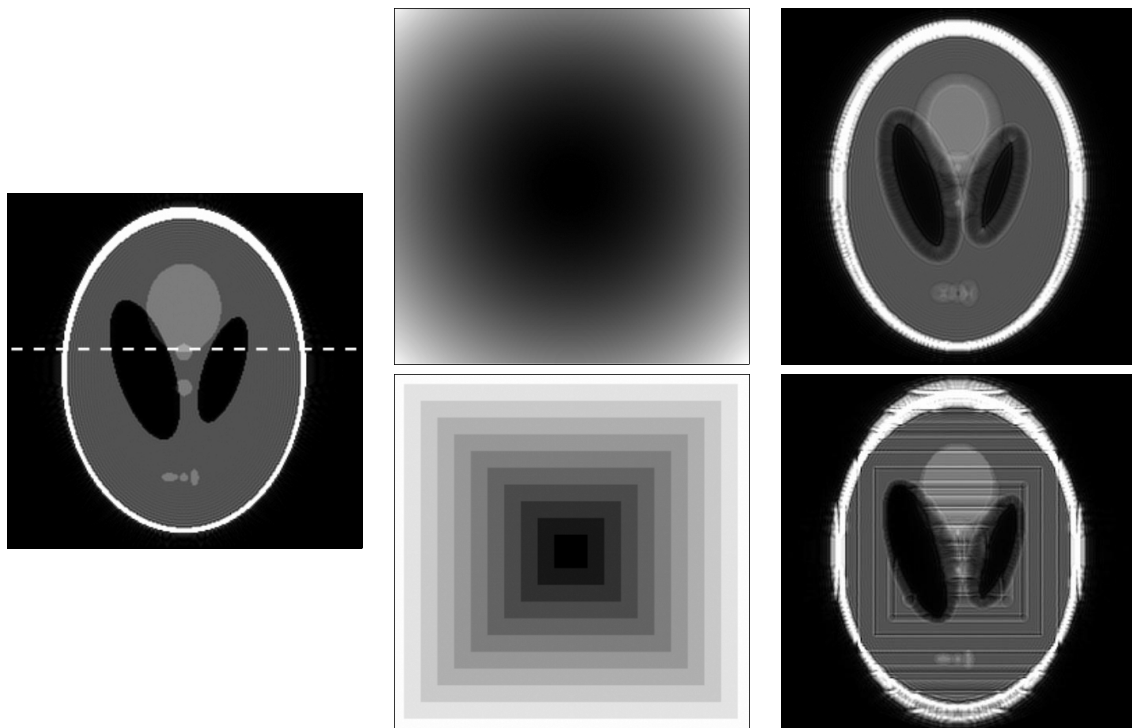
Fig. V.1. Image and field maps used in simulations. Shown are a filtered Shepp-Logan phantom on the left, a continuous, parabolic and a discrete, linear field map with off-resonance frequencies in the range of -125 Hz to +125 Hz in the middle, and results of a standard gridding reconstruction on the right. The latter were obtained from simulations of spiral k-space sampling and a readout duration of 32 ms. The dashed line superimposed on the phantom indicates the position where cross sections were taken for comparison.
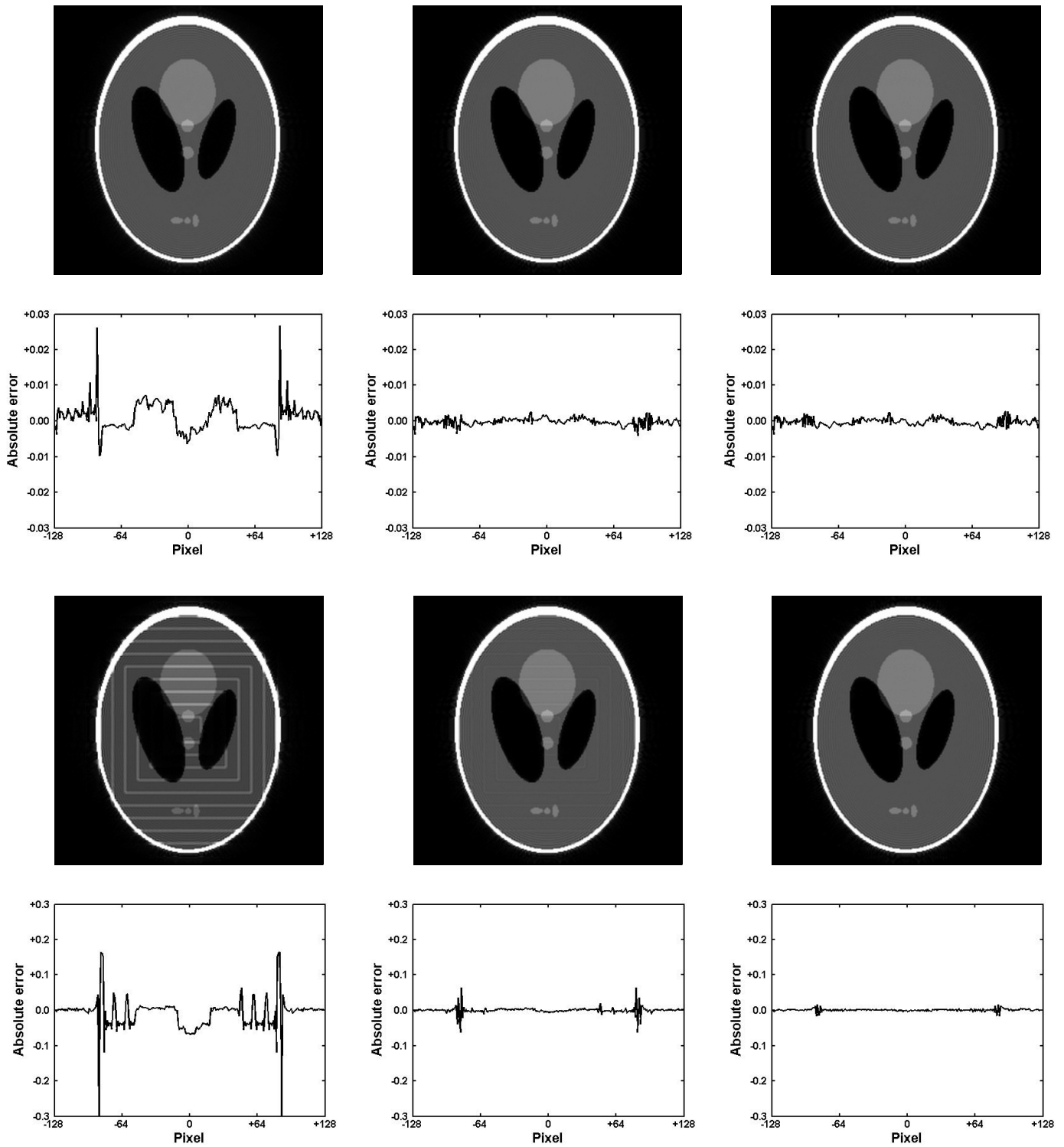
Fig. V.2. Results of simulations. Shown are intermediate images after 1, 2, and 3 iterations for the continuous field map at the top and after 1, 2, and 10 iterations for the discrete field map at the bottom. Below them, the differences to the original phantom are plotted for one cross section. The scaling varies by one order of magnitude between those at the top and those at the bottom.
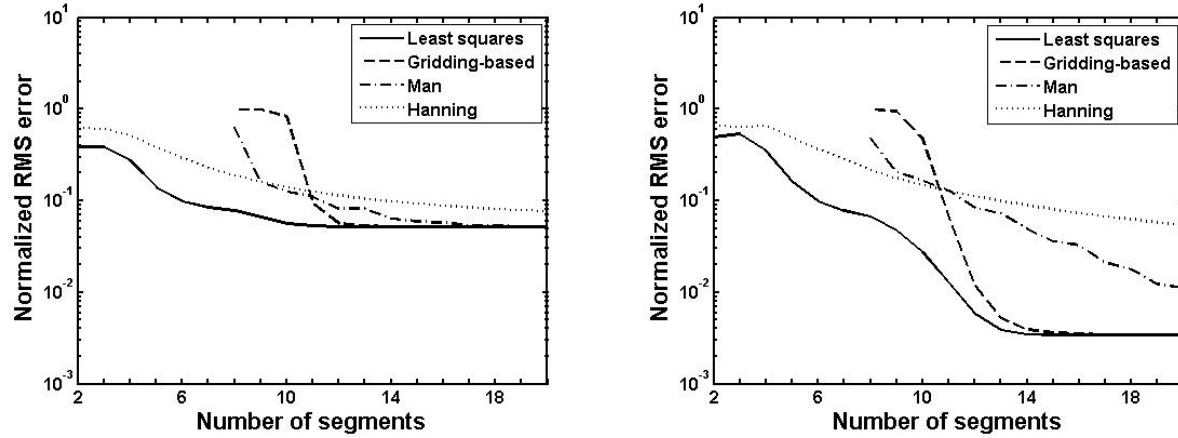
Fig. V.3.   Comparison of the accuracy of different correction algorithms. Plotted is the normalized root mean square (RMS) error as function of the number of segments in the interpolation after 1 and 3 iterations on the left and on the right, respectively.
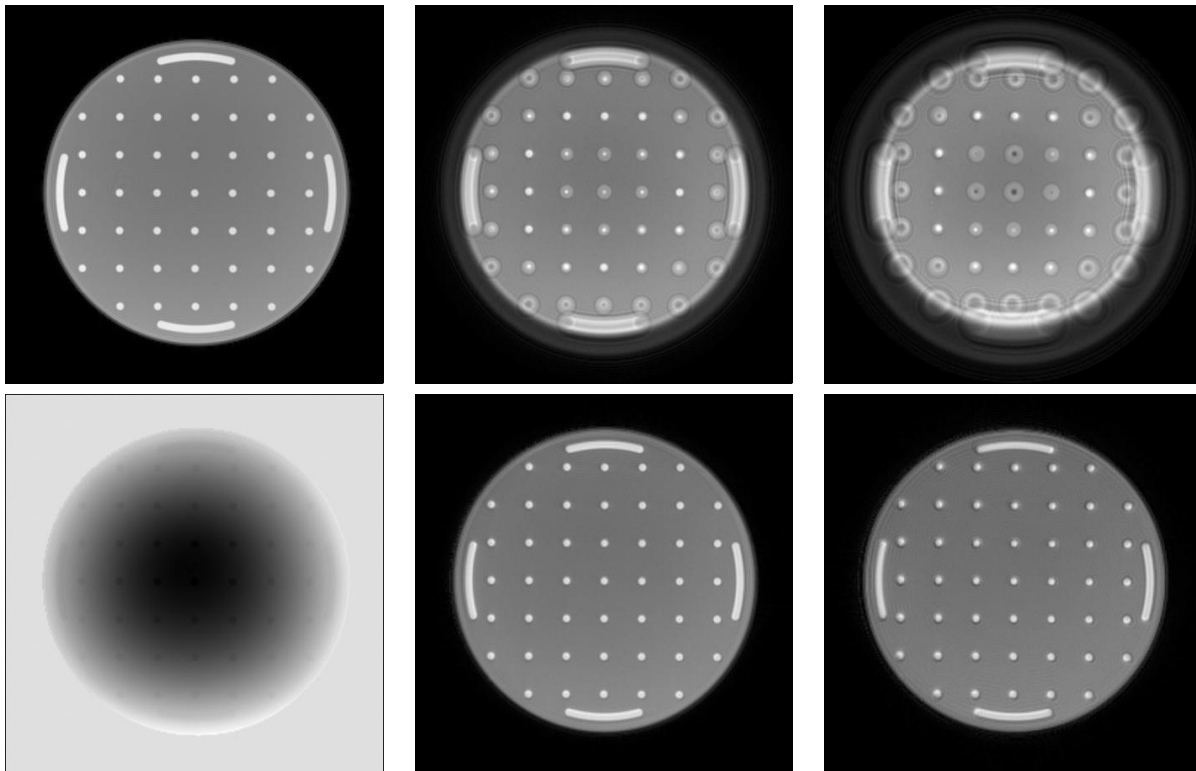

Fig. V.4.   Results of phantom experiments. Shown are a reference image and a field map obtained with Cartesian k-space sampling on the left, and two corresponding uncorrected and corrected images obtained with spiral k-space sampling. Those in the middle were measured with a readout duration of 28.5 ms, and those on the right with a readout duration of 56.5 ms.